Vol. 22, No. 3(2023) Mat2991
Revista Mexicana de Ingeniería Química

Influence on pretreatment in CeO_2 and Au/CeO_2 nanocomposite to improve the creation of surface defects enabling modification in optical interband

Influencia del pretratamiento en los nanocompuestos de CeO_2 y Au/CeO_2 para mejorar la creación de defectos superficiales que permitan modificar la interbanda óptica

M.X. Cordero-García*, E. Rojas-García, E. Salinas-Rodríguez, S. A. Gómez

Departamento de Ingeniería de Procesos e Hidráulica, Universidad Autónoma Metropolitana-Iztapalapa, Ciudad de México, 09340. México.

Received: October 25, 2022; Accepted: December 9, 2022

Abstract

In this work, we study the *in situ* behavior of CeO_2 and Au/CeO_2 during different pretreatments in temperature and atmosphere by Raman and UV-Vis diffuse reflectance. This procedure allows following in real-time the surface changes of Au nanoparticles and CeO_2. A logarithmic correlation between the CeO_2 lattice structural defects and the electronic states in the optical interband was obtained. In the case of Au/CeO_2, Au nanoparticles over the CeO_2 surface allow enhancing the properties formed by the electronic states between the valence band and the conduction band, increasing more than twice the structural defects compared to bare CeO_2. Furthermore, we verified that the conservation of oxygen vacancies is due to the pretreatment during a redox cycle. We emphasize the importance of the electronic properties of CeO_2 for a better understanding of the effect of pretreatments on Au/CeO_2 nanocomposite before its catalytic or photocatalytic applications.

Keywords: Cerium oxide, gold nanoparticles, *in situ* analysis, DR UV-Vis spectroscopy, Raman spectroscopy, band gap energy, Urbach energy.

Resumen

En este trabajo, estudiamos el comportamiento *in situ* de CeO_2 y de un nanocompuesto de Au/CeO_2 durante diferentes pretratamientos en temperatura y atmósfera mediante espectroscopías Raman y de reflectancia difusa en la región UV-Vis. Este procedimiento permite seguir en tiempo real los cambios estructurales que sufren las nanopartículas de Au y CeO_2. Se obtuvo una correlación logarítmica entre los defectos estructurales de la red de CeO_2 y los estados electrónicos en la interbanda óptica. Para el nanocompuesto de Au/CeO_2, las nanopartículas de Au en la superficie de CeO_2 mejoran las propiedades formadas por los estados electrónicos entre la banda de valencia y la banda de conducción, ya que incrementan al doble los defectos estructurales en comparación con CeO_2. Además, comprobamos que la conservación de vacancias de oxígeno se debe a la aplicación de pretratamientos bajo ciclos redox, resaltando la importancia de las propiedades electrónicas de CeO_2 para una mayor comprensión del efecto del pretratamiento de Au/CeO_2 antes de su uso como catalizador o fotocatalizador.

Palabras clave: óxido de cerio, nanopartículas de Au, análisis *in situ*, espectroscopía DR-UV-Vis, espectroscopía Raman, energía de banda prohibida, energía de Urbach.

*Corresponding author. *E-mail*: maraximena@gmail.com
https://doi.org/10.24275/rmiq/Mat2991
ISSN:1665-2738, *issn-e*: 2395-8472

1 Introduction

Cerium oxide is one of the most attractive rare earth oxides due to its redox properties, which have applications in diverse fields. However, redox processes alter the charge balance within the crystal lattice of CeO_2 creating a charge compensation acquainted as oxygen vacancies (Vo^{-}), which are responsible for the oxygen storage/release capacity (OSC) in its crystal lattice (Centeno *et al*., 2016). These characteristics have increased the potential of CeO_2 in applications such as fuel cells, solar cells, photocatalysis, and heterogeneous catalysis (Trovarelli and Fornasiero, 2013). Its cubic structure and fluorite type allow a load balance that promotes the decrease of the band gap energy (E_g). This allows to maintain the defect perturbations from Vo^{-}, which enables to obtain a material suitable for visible light or IR applications (Tiwari *et al*., 2019).

On the other hand, the study of metallic nanoparticles in nanocomposites has been developed since the 19th century because of their potential application in medicine, biomedicine, chemistry, catalysis, electronics, etc. It has been shown that in this scale the properties of a material become dependent on its size and shape (Eustis and El-Sayed, 2006; Willets and van Duyne, 2007). Catalysts with gold nanoparticles supported on cerium oxide are often used in different reactions such as CO oxidation, hydrocarbon combustion, and the water gas shift (WGS) reaction, among others (Freakley *et al*., 2015; Centeno *et al*., 2016). Usually, before their application, the nanocomposites are subjected to various pretreatments to obtain different active sites for the reaction of interest. Despite their applicability, there are few works with a detailed understanding of Au-based materials supported in oxide metals where is include the nature of active Au species, the reaction mechanism at the molecular scale, the physical origin of deactivation, and the influence of pretreatment for catalysis activation.

To reduce the discrepancy in the experimental works, it has been proposed a systematic study by the modification of a single parameter, while maintaining constant the material support, the preparation procedures, the pretreatment, and the reaction conditions (El-Moemen *et al*., 2016). For a detailed understanding of the role of the pretreatment to improve the catalytic activation, it is necessary to delve into the dynamic behavior of their reduction/oxidation states and their dependence on reaction preconditions in CeO_2 as a support and Au/CeO_2 catalysis (Schilling and Hess, 2018). Currently, some studies have analyzed the behavior of treatments in atmospheres at different temperatures, using spectroscopy techniques to elucidate the correlations between the structure and activity of the catalyst. Raman spectroscopy has excelled to know the behavior of Vo^{-} in both CeO_2 and Au/CeO_2 nanocomposites, due to its ability to quantitatively determine this phenomenon (Filtschew *et al*., 2016; Schilling and Hess, 2018).

Pushkarev *et al*. (2004), used Raman spectroscopy to detect Vo^{-} on CeO_2 by adsorbing molecular oxygen $^{16}O/^{18}O$ and by determining their behavior under pretreatments in H_2 and CO to reduce the sample. They observed a modification in the Vo^{-} caused by using a different reducer gas and suggested a different reduction mechanism. They propose that if CO is used as a reducer, an oxygen vacancy is formed adjacent to two Ce^{3+} ions and one CO_2 molecule. While the use of H_2 results in a water molecule and an oxygen vacancy adjacent to an OH group and a Ce^{3+} ion.

Zhang *et al*. (2011) have pointed out that CeO_2 is partially reduced in CO and gives rise to a promoter catalyst of oxidation resulting in a minimization of Vo^{-}. However, the formation of Vo^{-} is a key step in the formation of active sites, and it is preferable previously to treat samples with H_2 at high temperatures to obtain a partially reduced catalyst.

Regarding studies related to the redox behavior of the Au/CeO_2 nanocomposite and its structural changes in reducing or oxidizing atmospheres, Vindigni *et al*. (2011), reported an investigation of Raman *in situ* of Au/CeO_2 pretreated at 400 °C in O_2 and 100 °C in H_2. They observed the behavior of oxygen species, surface vacancies, and CeO_2 bulk. They also determined the presence of three types of Vo^{-}: i) inactive defects that react reversibly upon contact with O_2 forming peroxide-type species, ii) surface defects, created due to catalyst reduction and the presence of Au nanoparticles, and iii) internal CeO_2 defects attributed to the remaining Ce^{3+} species, which disappears at high temperature under oxidizing atmosphere.

Acosta-Silva *et al*. (2019) used CeO_2 from sol-gel synthesis to study the effect of temperature on the *in situ* structural properties generated or suppressed under an oxidizing atmosphere at 250, 350, and 450 °C by Raman and UV-Vis spectroscopies. They show that without reducing the catalyst the stress caused by temperature induction produces three types of vacancies (complexes), suggesting that raising the temperature also influences the creation of Vo^{-}.

In this work, we studied the behavior of CeO_2 and Au/CeO_2 nanocomposites in redox, optical, and electronic properties using *in situ* Raman and *in situ* diffuse reflectance UV-Vis spectroscopy to provide a fundamental understanding between the electronic states caused by the change of atmosphere and temperature for the creation of Vo^{-}, and to study the role of Au to increase the defects in the CeO_2 lattice. We demonstrate a direct correlation of CeO_2 lattice structural defects formed by electronic states in the optical interband.

2 Experimental section

2.1 Synthesis

2.1.1 Synthesis of CeO_2 nanoparticles

CeO_2 was synthesized via thermal decomposition of ammonium cerium (IV) nitrate ($(NH_4)_2$ $Ce(NO_3)_6$ Sigma-Aldrich, 98.5%) at 400 °C for 6 h in static air using a heating rate of 5 °C (Hernández *et al.*, 2015). The temperature ranges of these processes depend on the heating rate used since thermal decomposition occurs in two steps. At the beginning, at low temperatures, $Ce_2(NH_4)_3(NO_3)_9$ and gases are formed; then increasing the temperature yields only in CeO_2 and lofted gases. During the overall process the double valance charge of cerium occurs (Audebrand *et al.*, 1996).

2.1.2 Synthesis of Au/CeO_2

Au/CeO_2 was synthesized by the deposition-precipitation method described by Haruta *et al.* (1989) at room temperature, using a 0.013 M aqueous solution (S1) of tetrachloroauric (III) acid ($HAuCl_4{\cdot}3H_2O$ Sigma-Aldrich, 49.9% as Au). Corresponding to the nominal amount of 5 wt.%, S1 was added dropwise to a suspension with 5 g of CeO_2 in 50 mL of deionized water under stirring and preheated at 70 ºC. The initial pH was 2.8. Sodium hydroxide (NaOH) 0.1 M (J.T. Baker) was added to keep the pH at 7. After the addition of the solution, S1 was ended, and the mixture was aged 24 h at room temperature and then filtered. The solid obtained was dried at 120 °C for 2 h and, finally calcined at 400 °C for 4h in static air. It was shown that this procedure yields a homogenous distribution of Au nanoparticles between 2-20 nm (Haruta, 1997). Au content was determined by atomic absorption spectroscopy (Varian, Spectra AA-20FS).

2.2 Characterization methods

2.2.1 X-ray diffraction (XRD)

Powder X-Ray diffraction (XRD) was carried out in a Bruker D8 Advance equipment with Cu Kα radiation 2θ (λ = 0.15406 nm), measured from 15° to 108° with a step of 0.02°, for 76.8 s. The crystal structure of the samples was refined in Topas Academic code (v. 4.2) using the fundamental parameters approach (Coelho *et al.*, 2018). The program SRM-NIST 660b (LaB6) was employed to determine the instrumental contribution to the XRD patterns. Lattice parameters and average crystallite size were obtained by the Rietveld method.

2.2.2 Hydrogen Temperature programmed reduction (H_2-TPR)

Measurements were carried out in a reaction system ICID-2 (SRyC-2-México) from 25 to 1000 °C with a heating rate of 10 °C/min and a flow rate of 30 mL/min (10% H_2/Ar). The electric current of the TCD was 100 mA and the cell temperature at 100 ºC to avoid H_2O condensation.

2.2.3 Nitrogen physisorption

Nitrogen adsorption-desorption isotherms were obtained in a Quantachrome Autosorb 1 equipment at 75.2 K. Before the analysis the sample was degassed at 150 °C for 6 h at 30 mTorr, using 70 mg of the catalyst. The specific area calculated by applying the BET method was 18 m^2/g.

2.2.4 In situ UV-Vis diffuse reflectance

In situ spectra were recorded at room temperature on an Agilent Technologies Cary 5000 UV-Vis-NIR spectrophotometer, in the wavelength interval 185-2500 nm by using 30 mg of the samples in a reaction cell (Harrick Scientific). The samples were heated from room temperature to 400 ºC (reducing atmosphere) with a heating rate of 5 °C/min (Watlow 988 controller) at a flow rate of 20 cm^3/min with 5% H_2/N_2. Afterward, the samples were cooled to room temperature at the same flow rate with 5% O_2/N_2 (oxidizing atmosphere).

Table 1. Textural properties of CeO_2-UT and Au/CeO_2-UT.

Sample	d_c (nm)[1]	S_{BET} (m^2/g)	V_p (cm^3/g)	Au wt. %
CeO_2-UT	10.9	17	0.1729	-
Au/CeO_2-UT	15.8	15	0.1302	4.1

[1]Scherrer equation

Table 2. Average crystallite size, lattice parameter (a), and R_{wp} values for CeO_2 and Au/CeO_2 with their respective pretreatments.

Sample	Phase found	Percent phase	Average crystallite size (nm)	a (Å)	R_{wp}
CeO_2-UT	CeO_2	100	15.2	5.414	4.5
CeO_2-R-400	CeO_2	100	14.9	5.414	4.5
CeO_2-O-400	CeO_2	100	15.3	5.412	4.7
Au/CeO_2-UT	CeO_2	95.6	16.4	5.413	4.8
	Au	4.1	22.8	4.076	
Au/CeO_2-O-400	CeO_2	95.9	15.7	5.412	4.6
	Au	4.1	25.8	4.076	
Au/CeO_2-R-400	CeO_2	95.95	15.4	5.412	4.5
	Au	4.05	22.9	4.077	

2.2.5 *In situ Raman spectroscopy*

Reduction cycles were measured using the same conditions used during *in situ* DRS UV-vis in a micro-Raman in Via equipment Renishaw with a Linkam reaction cell, in the interval 100 - 3000 cm^{-1} (532 nm laser excitation and 20x objective magnification). The equipment was calibrated with Si^0. To avoid damage produced by the laser beam, the laser power was adjusted to 1 mW (1%). There were three accumulations for each sample with 10 s of exposure time. A controller (Watlow 988) was used to increase the temperature from 25 to 400 ºC with a heating rate of 5 °C/min.

3 Results and discussion

In what follows, the nanocomposites shall be labeled as sample-UT for untreated, after reduction at the respective temperature as -R-T or as -O-T for samples treated in oxidizing atmosphere.

The Au loading for the Au/CeO_2-UT nanocomposite was determined by atomic absorption spectroscopy (AAS) and corresponds to 4.1 wt.%. Crystallite size (d_c) calculated by the Scherrer equation, BET specific surface (S_{BET}), and pore volume (V_p), are summarized in Table 1.

3.1 *Preservation of the CeO_2 structure in both CeO_2 and Au/CeO_2 samples after reductive and oxidative pretreatments*

As it is well known, power X-Ray diffraction patterns of CeO_2-UT correspond to that of fluorite structure (JCPDS- 81-0792). Characteristic peaks are located at 2θ = 28.5, 36.4 and 44° which correspond to (111), (200), (220) lattice planes respectively (Varez *et al.*, 2006). These are also present in the *ex situ* XRD patterns of samples CeO_2-R-400 and CeO_2-O-400. Moreover, the characteristic peaks of Au, which are located at 2θ = 39, 44.1, and 64.3°, correspond to (200) and (220) lattice planes, respectively (JCPDS 4-0783).

For CeO_2, the unit cell was modeled with the cubic symmetry described by the *Fm-3m* space group (#225), and a basis containing one Ce^{4+} at the relative coordinates (0, 0, 0) and one O^{2-} at the relative coordinates (1/2, 1/2, 1/2) (Varez *et al.*, 2006). Au was also modeled with the cubic symmetry described by the Fm-3m space group (# 225) and a basis containing one Au at the relative coordinates (0, 0, 0) (Rösken *et al.*, 2014). Data were calculated through the diffraction peak 2θ = 28.5°, corresponding to the (111) lattice plane of CeO_2. In Figures 1 and 2, experimental and Rietveld refinement parameters of CeO_2 and Au/CeO_2 nanocomposites are shown.

From Table 2, it is noted that the average crystallite size and the lattice parameter of CeO_2 are modified, depending on the atmosphere either as reducing or oxidizing. Deshpande *et al.* (2005) observed that the

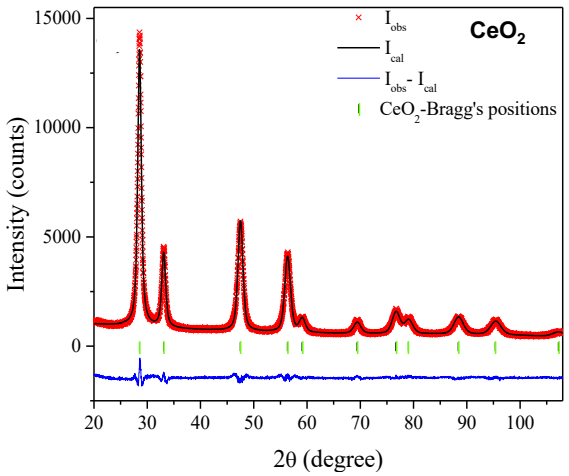

Figure 1. Rietveld refinement plot of representative CeO_2-UT. The x mark and the upper solid line correspond to the experimental and calculated data, respectively. The lower blue curve is the difference between them. The vertical marks on the bottom, represent the Bragg reflections associated with CeO_2 with the cubic-like structure.

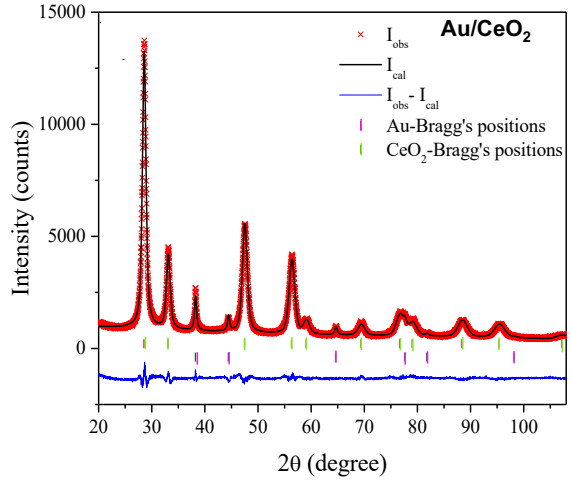

Figure 2. Rietveld refinement plot of representative Au/CeO_2-UT. The x mark and the upper solid line correspond to the experimental and calculated data, respectively. The lower blue curve is the difference between them. The vertical marks on the bottom, represent the Bragg reflections associated with CeO_2 and Au.

fraction of Ce^{3+} increases with decreasing particle size, which is related to a higher concentration of Vo^{-}. In addition, the higher the Ce^{3+} concentration, the higher the lattice strain, with changes in crystal size or lattice parameter. The low R_{wp} values around 4.5, indicate a good adjustment between experimental and calculated values. The obtained values are in accordance with those reported by Hernández *et al.* (2015) and Acosta-Silva *et al.* (2019) for Au/CeO_2. The crystallite size of Au/CeO_2-UT is greater than CeO_2-UT, which suggests a change in the crystalline structure due to the deposition of Au-nanoparticles (Au-NP) on the CeO_2 surface.

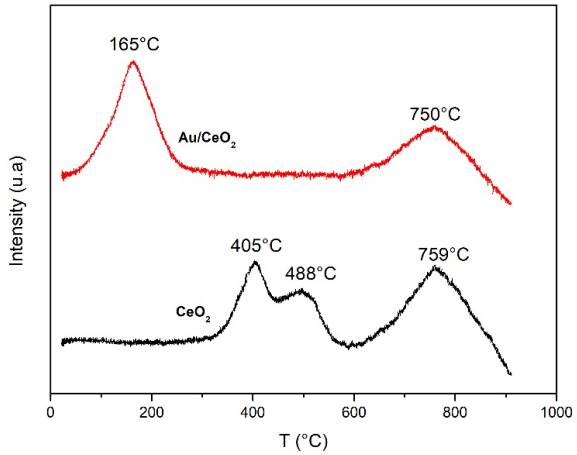

Figure 3. TPR-H_2 reduction of CeO_2 -UT and Au/CeO_2 -UT nanocomposite.

From Rietveld refinement, the average of crystallite size (d_c) and the lattice parameter of cubic CeO_2 (a_0) was obtained, and our results confirm a slight modification of those parameters depending on the pretreatment applied (reduction or oxidation). These results also indicate that *ex situ* XRD does not give sufficient information on the structural changes that occur during reductive or oxidative pretreatments, and to detect possible modifications in the lattice parameter and deformation. Therefore, *in situ* studies are necessary to determine the effect of atmosphere and temperature on these parameters.

On the other hand, Figure 3 shows the H_2-TPR patterns of CeO_2-UT and Au/CeO_2-UT samples. The CeO_2-UT reduction pattern shows two peaks at low temperatures (405 and 488 °C) assigned to the surface reduction of CeO_2, and one peak at high temperature (>759 °C) which is attributed to the bulk reduction of CeO_2 (Trovarelli and Fornasiero, 2013; Huang *et al.*, 2009). While for 4.1 wt.% Au/CeO_2/RT, $Au^{\delta+}$ species and CeO_2 surface oxygen reduced simultaneously at 165 °C (Zhang *et al.*, 2011; Hernández *et al.*, 2015). During this reduction process, a change in the Ce^{3+}/Ce^{4+} ratio and the creation of Vo^{-} occur. These changes should change the CeO_2 lattice parameter that was not detected by the *ex situ* XRD of the samples.

The reduction of $Au^{\delta+}$ species follows the sequence $Au^{+3} \rightarrow Au^{+1} \rightarrow Au^{0}$. This has been related to determine the catalytically active species for oxidation reactions. Chang and Sheu (2016) suggested that Au^{+3} species are non-active; however, Widmann *et al.* (2007) claimed that Au^{0}-NP are responsible for O_2 activation, while $Au^{\delta+}$ species promote the conversion of CO to CO_2. Therefore, the active sites on Au/CeO_2 nanocomposites remain controversial (Karpenko *et al.*, 2007). Therefore, the use of pretreatment of the catalyst could be relevant to establish a correct balance between Au species and Au^{0} in CeO_2, before performing a specific catalytic reaction (Zhang *et al.*, 2011).

3.2 *Evidence of changes in Ce^{3+}/Ce^{4+} during pretreatments via in-situ DR UV-Vis studies*

DR UV-Vis spectroscopy allows surface information for metal oxides and supported metals (Guo *et al.*, 2011). *In situ* DR UV-Vis spectra of samples are presented in terms of the Kubelka Munk function (F(R)). It is an inverse function of the reflectance (%R) and relates the intensity of light detected and the amount of light reflected on the surface of the sample (Schoonheydt, 2010). The spectra were obtained from *in situ* pretreatments of CeO_2 during a cycle from 25 to 400 °C of reducing atmosphere (R), followed by treatment from 400 to 25 °C in an oxidizing atmosphere (O) (Figure 4).

All spectra present bands between 200 and 500 nm with a maximum at 350 nm and a shoulder at 288 nm which are attributed to Ce^{4+} and Ce^{3+} species, respectively (Huang *et al.*, 2009). The change in intensity as temperature increases is attributed to the lattice modification of CeO_2 due to charge transfer from the O^{2-} valence band to Ce^{4+} 4f band (Reina *et al.*, 2014; Schilling and Hess, 2018). For Au/CeO_2 nanocomposite, the same bands related to Ce^{4+} and Ce^{3+} (360 and 288 nm) appear from CeO_2 with a broad band at 560 nm attributed to the gold surface plasmon (SP) (Figure 5). The SP due to the optical response of electron movement in metal nanoparticles (NP) caused by incident light excitation (Eustis and El-Sayed, 2006), is unequivocally attributed to the presence of Au^{0}-NP (Willets and van Duyne, 2007; Eustis and El-Sayed, 2006; Schilling and Hess, 2018).

During exposure to a reducing atmosphere, the Au-SP band increases, which implies the reduction of $Au^{\delta+}$ species in Au/CeO_2 (Figure 5). Moreover, according to the reduction process in CeO_2, the charge of the bands assigned to $Ce^{4+} \rightarrow Ce^{3+}$modifies, if the Ce 4f band is filled. This leads to an electronic exchange between Ce 4f "*full*" and Au^{0}-NP (Acosta-Silva *et al.*, 2019). Also, the continuous increase in temperature directly affects the internal reduction (bulk) of CeO_2 and full width at half maximum increases. These changes could be related to the creation of Vo^{-}, which leads to the expansion in the CeO_2 lattice due to the substitution of Ce^{4+} ions by Ce^{3+} species (Acosta-Silva *et al.*, 2019).

On the other hand, the treatment with an oxidizing atmosphere (5% O_2/N_2) transitions from "*full*" Ce 4f to an "*empty*" Ce 4f structure prevail corresponding to the decrease of Ce^{3+} species, to return reversibly to species Ce^{4+} (Filtschew *et al.*, 2016). This charge transfer reflects changes in the Au-SP such as a redshift, and the decrease in intensity could be reflected in the loss of Au^{0} species by reoxidation (Hernández *et al.*, 2015; Schilling and Hess, 2018). In general, the DR UV-Vis spectra are quite similar for both pretreatments. However, it is relevant to quantify the Au-SP and the Ce^{3+}/Ce^{4+} ratio since our results show that in both cases Vo^{-} are created. Nevertheless, in an oxidizing atmosphere, a fraction of Au^{0} species is lost, which may affect the catalytic activity. These results are difficult to demonstrate when nanocomposites are evaluated by *ex situ* conditions (Huang *et al.*, 2009).

Both Ce^{3+}/Ce^{4+} ratio and the E_g are calculated from the DR UV-Vis spectra. CeO_2 spectrum also shows a redshift at the absorption edge as a function of temperature and atmosphere (Figure 6).

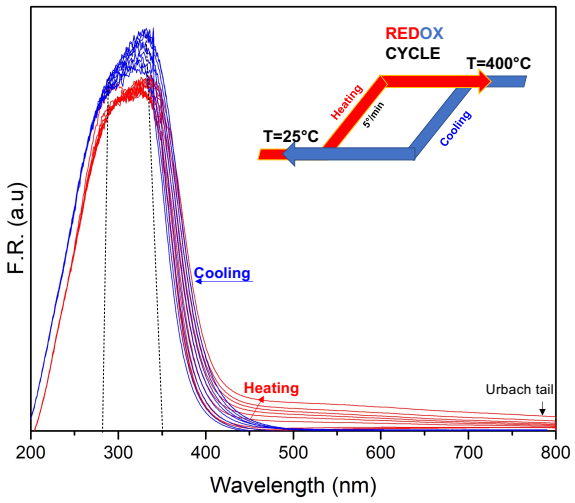

Figure 4. DR UV- Vis in situ of CeO_2 in a redox cycle at different temperatures.

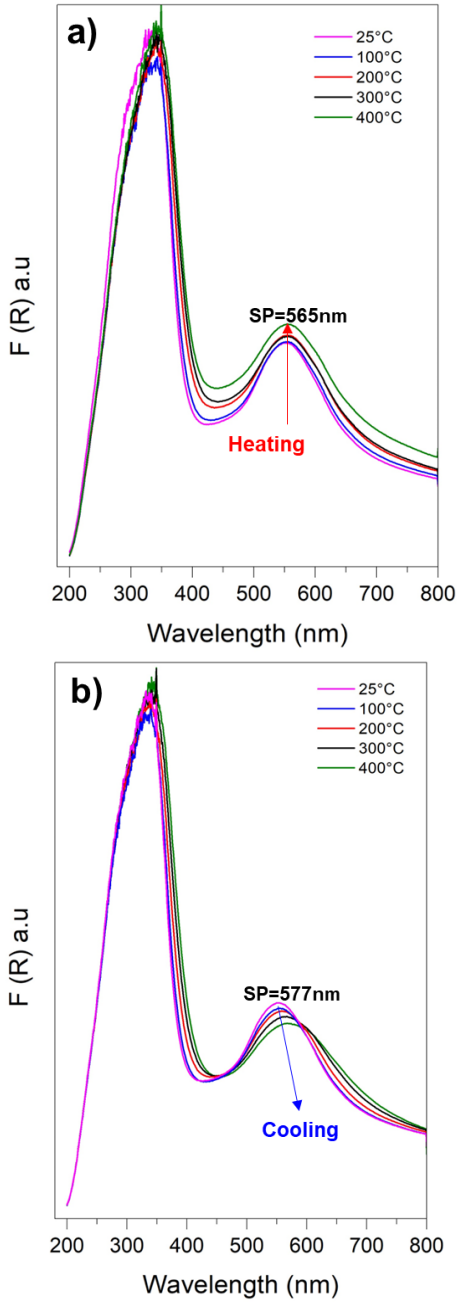

Figure 5. DR UV-Vis *in situ* spectrum of Au/CeO_2 from 25 °C until 400 °C under (a) reducing and (b) oxidizing atmosphere.

These modifications correspond to exponential tails at the edges of the optical interband located between the valence band and the conduction band known as the Urbach tails, resulting from short hybrid excitonic transitions, and are related to lattice parameter deformation (Boubaker, 2011). Calculations show that

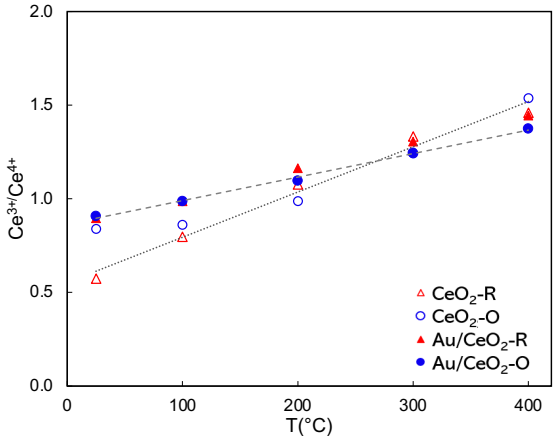

Figure 6. Variation on Ce^{3+}/Ce^{4+} ratio at different atmospheres and temperatures.

Ce^{3+} /Ce^{4+} ratio increases and decreases linearly in reducing and oxidizing atmospheres, respectively. Although, at the end of the redox cycle the value of Ce^{3+}/Ce^{4} is different (Figure 6); since this overall process increases the reducibility of CeO_2 to create vacancies by applying redox cycles with the reduction of CeO_2 at high temperature and subsequently re-oxidize it (Trovarelli and Fornasiero, 2013). Moreover, the slope value indicates that the process for CeO_2 support and Au/CeO_2 nanocomposite is not the same, giving evidence that Au modifies the amount of Ce^{3+} ions present in CeO_2. According to our results, the application of redox cycles partially reduced CeO_2 and create a certain number of vacancies depending on the atmosphere used and temperature.

Information on the specific band edge energy can be obtained from the UV region by obtaining E_g (Ovando-Medina *et al.*, 2018; Huang *et al.*, 2009). It was estimated from the modified Kubelka-Munk equation $[F(R_\infty)h\nu]^{1/\eta}$ *vs.* incident energy (Figure 7) where R_∞ is the percentage of reflected light (Eq. 1)

$$F(R_\infty) = \frac{(1-R_\infty)^2}{2R_\infty} = \frac{\alpha(\text{absorption coefficient})}{S\,(\text{scattering coefficient})} \quad (1)$$

and $h\nu$ is the incident photon energy. For each transition, η takes specific values: direct allowed (1/2), direct forbidden (3/2), indirect allowed (2), and indirect forbidden (3) (da Silva *et al.*, 2015). E_g of CeO_2 was calculated with indirect and direct transitions, however, the most common values are obtained by considering an indirect allowed transition (η = 2), which results in E_g between 2.6 - 3.4 eV (Choudhury *et al.*, 2015; da Silva *et al.*, 2015; Filtschew *et al.*, 2016).

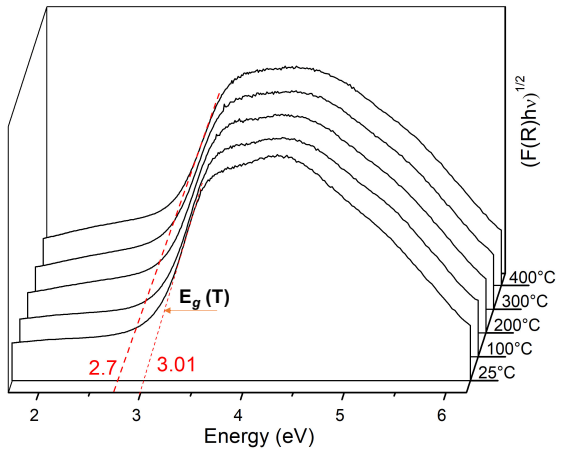

Figure 7. Band gap (E_g) plot from Kubelka Munk function $(\alpha h\nu)^{1/2}$ *vs*. the incident energy (eV) of CeO_2 in a reducing atmosphere at different temperatures.

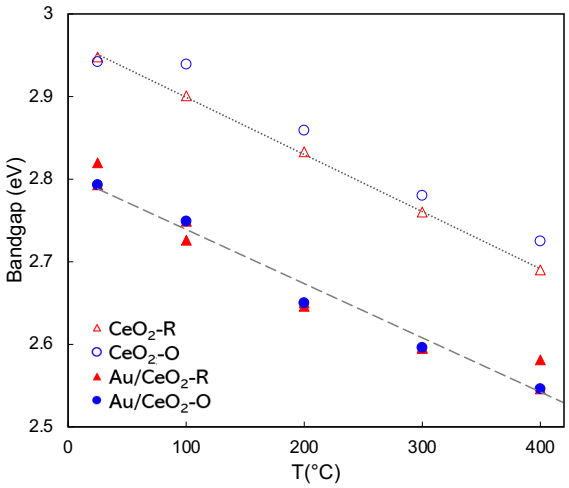

Figure 8. Band gap behavior of CeO_2 and Au/CeO_2 nanocomposite at different atmosphere and temperature.

Figure 8 presents the E_g values for CeO_2 and Au/CeO_2 as a function of temperature and atmosphere. It is observed that for both samples, as temperature increases, E_g decreases linearly with a similar slope, suggesting that both Vo^- and Ce^{3+} ions are responsible for this behavior. However, with the presence of Au metal nanoparticles, E_g decreases 10% more than in the case of CeO_2. Barton *et al*. (1999) and, Eustis and El-Sayed (2005) propose that this reduction in E_g implies that the material becomes more conductive; indicating the possibility of some anionic Vo^- on the surface as these induce the formation of surface oxygen at the Au-CeO_2 interface. Then, the role of Au is to act as an electron donor/acceptor, and consequently, E_g decreases, and the PS band of Au metal nanoparticles increases. This implies that the Au-NP reduce CeO_2 and minimizes the distance of higher energy levels (Hernández *et al*., 2015). Moreover, this directly influences the catalytic activity as it minimizes the oxygen energy levels and allows electron transfer between the oxygen atoms of CeO_2 and Au (Huang *et al*., 2009) inducing a strong electronic interaction between the metal and the support (Reina *et al*., 2014).

The Urbach energy (E_u) can be calculated from the relation (Eq. 2) (Thill *et al*., 2020):

$$\alpha = (\alpha_o)\exp\frac{(h\nu - E_g)}{E_u} \tag{2}$$

α_o is a material-dependent constant, E_g and E_u are given in eV. The optical absorption coefficient (α) is important since it determines the photocatalytic activity of the CeO_2. It is obtained through the Kubelka-Munk equation. Furthermore, according to Barton *et al*. (1999), F(R) can be represented as α in (Eq. 1) to obtain the values of E_u (Eq. 3):

$$\ln(\alpha) = \ln(\alpha_o) + \frac{(h\nu - E_g)}{E_u} \tag{3}$$

Figure 9 indicates a linear correlation between E_u and E_g which has been observed in several semiconductors (Hassanien and Akl, 2016). Consequently, from our results, the increase in E_u or the decrease in E_g, in both CeO_2 and Au/CeO_2, is due to the creation of disorder states and defects in the CeO_2 lattice during redox cycling at different temperatures. These defects are considered Vo^-, which arise due to Ce^{4+} reduction and thermal disorder induced by temperature change (Choudhury *et al*., 2015).

3.3 Determination and quantification of CeO_2 and Au/CeO_2 lattice defects

In situ Raman spectroscopy was used to obtain information on the interaction between Ce^{3+} and Ce^{4+} ions to form the defects or Vo^- in CeO_2 and Au/CeO_2. Figure 10 shows the Raman spectra of CeO_2 treated in a reducing and oxidizing atmosphere in the interval 25 - 400 ºC.

Figure 10 shows the typical bands of CeO_2. The main band at 462 cm^{-1} (F_{2g} mode) corresponds to the cubic fluorite structure (Kosacki *et al*., 2002; Pushkarev *et al*., 2004; Filtschew *et al*., 2016; Sartoretti *et al*, 2019). The band at 250 cm^{-1} is attributed to the second-order transverse acoustic

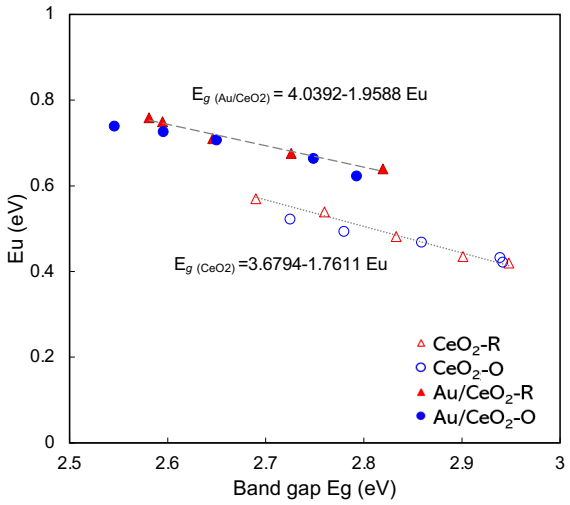

Figure 9. Linear relationship between E_g and E_u for a different atmosphere and temperature.

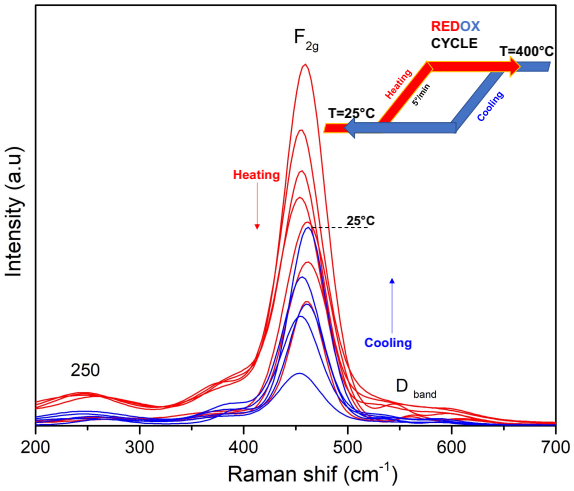

Figure 10. Raman spectrum of CeO_2 *in situ* from 25 °C to 400 °C by applying redox cycle at different temperatures.

mode (2TA) (Daniel and Loridant, 2012), although it has also been assigned to the oxidation state of CeO_2 (Guo *et al*., 2011; Schilling and Hess, 2018). Finally, the "D" defect-induced band observed in the interval 550 - 600 cm^{-1} is the result of the relaxation of symmetry selection rules caused by structural defects in the cubic lattice of CeO_2 (Lykaki *et al*., 2018), which results in the formation of different types of Vo^{-} (Kosacki *et al*., 2002, Pushkarev *et al*., 2004, Filtschew *et al*., 2016, Acosta-Silva *et al*., 2019).

The nature of the vacancies remains a current topic of discussion. However, there is an agreement about the existence of surface or extrinsic vacancies, which have been related to impurities or doping agents, to bulk or intrinsic vacancies due to the change of temperature or the atmosphere used (Trovarelli and Fornasiero, 2013). In addition, Frenkel-type defects occur due to the movement of the oxygen atom to an interstitial position (Sartoretti *et al*., 2019).

As we can see in Figure 10, the *in situ* Raman spectra of CeO_2 depend on the temperature (25-400 ºC) and pretreatment (reduced or oxidized) used. In a reducing atmosphere, the band at 250 cm^{-1} intensifies, whereas in an oxidizing atmosphere it decreases considerably. These results give evidence of the modification of the Ce^{3+}/Ce^{4+} ratio (Guo *et al*., 2011). This figure also shows the predominance of defect intensity in a reducing atmosphere, a pronounced drop of the F_{2g} peak, and the minimization of oxygen defects (D band) in the oxidizing atmosphere.

The most intense band at 462 cm^{-1} shows a red shift as the temperature increases until a value of 454 cm^{-1} at 400 °C is reached. This behavior is attributed to the reduction of the CeO_2 surface by the creation of Vo^{-} and the transfer of electrons from Ce^{4+} to Ce^{3+} (Schilling Schilling and Hess, 2018). When the atmosphere changes to an oxidant we observe a blue shift of the F_{2g} band, and it returns exactly to its original position as initially. This behavior was reported by Sartoretti *et al*. (2019, 2020) demonstrating total reversibility where the CO or H_2 atmosphere does not significantly affect the structure of CeO_2 (Figure 11). Instead, the generation of Vo^{-} (defects) occurs due to the rapid conversion of Ce^{4+} to Ce^{3+} to maintain the neutral charge due to the ion displacement which is affected by the movement of O^{2-} caused by the increase of temperature during the reducing treatment (Trovarelli and Fornasiero, 2013; Vindigni *et al*., 2011; Schilling and Hess, 2018).

Calculation of defects produced in CeO_2 was obtained from the IF_{2g}/I_D or AF_{2g}/A_D ratio. The bands in the spectra are slightly shifted due to the thermally induced strain, while the band broadening is due to the lattice perturbation effects on CeO_2 (Vignidi *et al*., 2011). As it is considered in the description for Vo^{-}, the D-band at 540 cm^{-1} corresponds to the movement of an O^{-} atom to an octahedral interstitial position due to the presence of Ce^{3+} ions which generates a vacancy (Zhang *et al*., 2011). This vibrational feature can be considered an "*extrinsic*" defect (Sartoretti *et al*., 2019). The band at 590 cm^{-1} may be due to defects arising from the presence of anionic or Frenkel defects (Agarwal *et al*., 2013; Sartoretti *et al*., 2019).

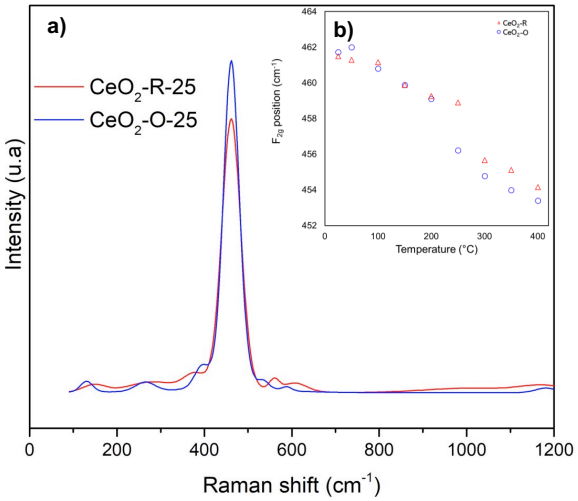

Figure 11. Comparisons between (a) the *in situ* Raman spectra of CeO_2-R-25 measured at the beginning, and CeO_2-O-25 at the end of the redox cycle, and (b) F_{2g} position during the redox cycle.

In general, *in situ* Raman study indicates that CeO_2 in reducing atmosphere ID/IF_{2g} ratio increases with temperature, from 0.044 at 25 °C to 0.16 at 400 °C; similarly, it decreases upon cooling in the oxidizing atmosphere from 0.018 at 400 °C to 0.013 at 25 °C. This confirms that reducing the atmosphere increases the O_2 vacancies (Vindigni *et al*., 2011).

For Au/CeO_2, there is a widespread opinion that Vo^{-}, plays a crucial role in binding the catalytically active species on CeO_2 (Centeno, 2016), which have a strong influence on the Au-NP. Furthermore, Au is considered the active site of the nanocomposite since these particles are deposited close to the Vo^{-}, (Vindigni *et al*., 2011). It has been also suggested that Au-NP are in direct interaction with the Ce (111) surface allowing a charge transfer from the support to the Au-NP during the reduction process encouraging the reoxidation process (Widmann *et al*., 2007).

Figure 12 shows Au/CeO_2 nanocomposite in a reducing atmosphere, where the same bands as in the CeO_2: 230, 464, and 545 - 590 cm^{-1} are observed. The latter band is related to the interaction between Au nanoparticles dispersed on the surface with the CeO_2 particles, to form an oxygen vacancy (Lee *et al*., 2011; Lakshmanan *et al*., 2013). It is considered that the reduction of the nanocomposite increases the creation of Vo^{-}, due to the electron transfer from the metal nanoparticles and the presence of H_2 (Vindigni *et al*., 2011). The decrease in the intensity is related to the decrease of the particle size and the increase

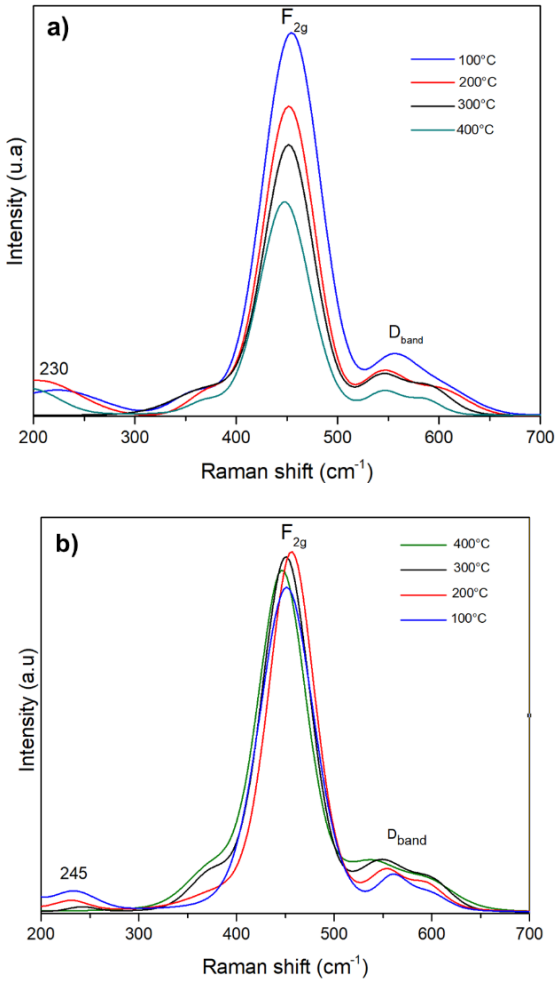

Figure 12. Raman *in situ* spectrum of Au/CeO_2 from 25 °C to 400 °C under (a) reducing, and (b) oxidizing atmospheres.

of the temperature. On the other hand, changing from a reducing to an oxidizing atmosphere, the intensity of the F_{2g} band decreases due to the loss of surface oxygen caused by the defect regeneration (Ziemba *et al*., 2021); after returning to room temperature the intensity of the F_{2g} band is restored.

Although the intensity of the D-band decreases, it does not disappear completely, which leads us to infer that part of the defects is preserved due to this redox process (Trovarelli and Fornasiero, 2013). We suggest these defects may still be present without further sample reduction. The ID/IF_{2g} ratio for Au/CeO_2 nanocomposite results to be 0.39 at 400 °C in a reducing atmosphere and 0.10 at 25 °C in an oxidizing atmosphere; these values are at least twice greater than those obtained by the reduced CeO_2 at the same

temperature. Therefore, the highest number of defects is obtained for Au/CeO_2 nanocomposite.

3.4 Evidence of the relationship between structural defects and minimization in optical interband

It is considered that Ce^{3+} species are responsible for creating the modifications in the localized electronic states and in band structure which result in electronic transitions assisted by phonons (Tiwari *et al*., 2019). Since Vo^{-} modify the states closer to the band edge, the increase of Vo^{-}, results in a decrease of E_g and an increase of E_u; and therefore, the creation of defects. Lattice distortion and reduction of Ce^{4+} to Ce^{3+} greatly modify the band structure of CeO_2 due to the reducing atmosphere and an increment in temperature. Accordingly, Vo^{-}, give a red shift and minimize the E_g from the UV to the visible region, as observed in Figure 4.

The presence of Ce^{3+} induces a structural disorder with stress at the bonding network of the atoms present in the crystalline structure of CeO_2. Also, these network stresses increased after CeO_2 was subjected to a reducing atmosphere at 400 °C (Deshpande *et al*., 2005); this agrees with the results obtained by XRD. Thill *et al*. (2020) demonstrated that an increase in the lattice parameter of a crystalline CeO_2 sample implies a higher fraction of Ce^{3+}. From these findings, we obtain for the first-time direct evidence that the lattice structural defects of CeO_2 take place from the modifications formed by the electronic states between the valance and the conduction bands.

Figure 13 shows the logarithmic behavior of the localized band states in the creation of Vo^{-}; the results in reducing atmosphere were considered, including CeO_2 support and the Au/CeO_2 nanocomposite. As mentioned above, the creation of Vo^{-}, leads to a decrease in E_g, which is directly dependent on the operating temperature. Furthermore, the presence of Au metal NP not only decreases E_g due to their electron acceptance but also significantly increases the number of structural defects in the CeO_2 lattice. This involves an increase in E_u allowing the expansion of the mind gap and an improvement in photocatalytic activity (Yaghoubi *et al*., 2015).

Raman spectroscopy was used to evaluate the oxygen vacancy concentration at the surface of the samples as a function of the grain size. It is considered the correlation (Eq. 4) proposed by Weber and

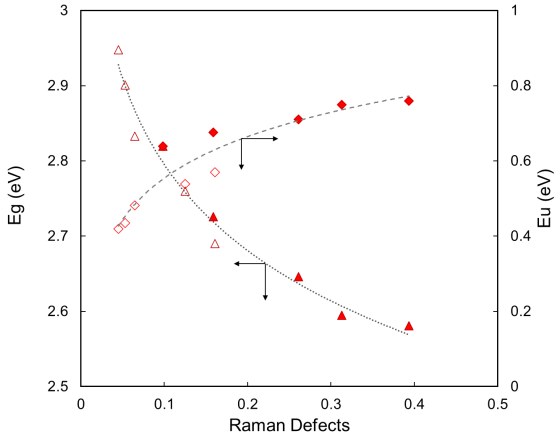

Figure 13. Correlation between the optical interband (E_g & E_u) and the produced surface Raman defects. The open marks correspond to CeO_2-R and the filled marks correspond to Au/CeO_2-R.

McBride (1993), for the F_{2g} peak of CeO_2 (465 cm^{-1}).

$$d_g(nm) = \frac{51.8}{(HWHM - 5)} \tag{4}$$

$HWHM$ is the half-width at half-maximum of the grain size. The defect concentration N (cm^{-3}) is calculated from (Eq. 5),

$$N = \frac{3}{4\pi L^3} \tag{5}$$

L (nm) is the correlation length (average distance between two lattice defects) defined in (Eq. 6).

$$L(nm) = \sqrt[3]{\left(\frac{a}{2d_g}\right)^2 \left[(d_g - 2a)^3 + 4d_g^2 a\right]} \tag{6}$$

a (= 0.34 nm) is CeO_2 radius, obtained from universal constants (Trogadas *et al*., 2012). Figure 14 shows the oxygen vacancy concentration N of the samples as a function of d_g, for Au/CeO_2-R and Au/CeO_2-O samples at temperatures between 25 and 400ºC. These data can be adjusted to a logarithmic curve with a 0.998 correlation value. In Figure 14 this logarithmic correlation shows that the grain size increases when the number of vacancies in CeO_2 and the Au/CeO_2 nanocomposites decreases. These vacancies decrease in contact with an oxidizing atmosphere and as the temperature decreases. However, these CeO_2 vacancies reach concentration ranges of 10^{21} cm^{-3} and correspond to the formation of conductive filaments (Gunkel *et al*., 2020). The concentration of the Vo^{-} on the surface behavior of the nanocomposites

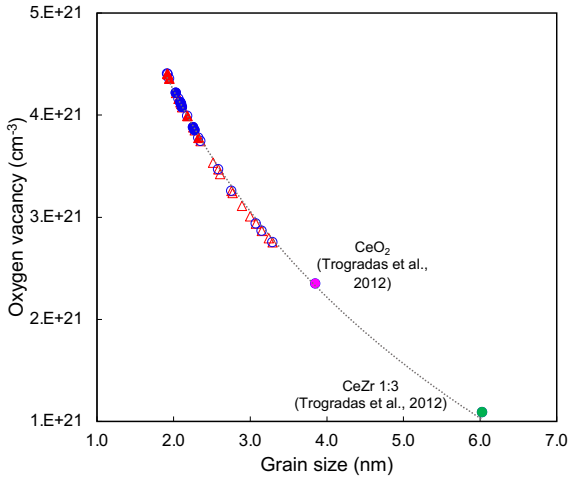

Figure 14. Relation between the grain size and the number of oxygen vacancies created in CeO_2 and Au/CeO_2 at different atmosphere and temperature.

follows the trend Au/CeO_2-R ≥ Au/CeO_2-O > CeO_2-R ≥ CeO_2-O ≥ CeO_2 and the grain size of the nanoparticle diminishes.

It is important to emphasize that this curve also predicts the value due to vacancies related to a doped sample with zirconia (Trogadas *et al.*, 2012) with high relevance. These authors concluded that the minimization of the number of Vo^{-}, enhances the generation of photoluminescent materials since they are associated with trapped electrons and maintain exciting electrons trapped in non-radiative centers that decrease the photoluminescent intensity (Choudhury *et al.*, 2015). In consequence, the potential use of CeO_2 as a material has been investigated during the last few years. This is due to the capability of host intrinsic factors on photon downshifting from near UV to the NIR to enhance the efficiency of photovoltaic solar cells for the solar spectrum adaptation (Padilla-Rosales *et al.*, 2020). Furthermore, the decrease in photoluminescent intensity provides an opportunity to obtain an active material for photocatalytic applications (Yaghoubi *et al.*, 2015; Thill *et al.*, 2020).

Conclusions

In summary, the dynamic of the pretreatment of CeO_2 and Au/CeO_2 during redox cycles with reducing or oxidizing atmosphere at different temperatures is understood with Raman and UV-Vis *in situ* spectroscopies. These techniques allow us to follow the optical and electronic modifications of the surface and subsurface of CeO_2 that result in the formation of Vo^{-}. The increase of Vo^{-} allows an active material for catalytic and photocatalytic applications, while its minimization implies obtaining a material with photoluminescent properties.

Our results allowed us to obtain for the first time a correlation describing the behavior of gap and Urbach energies depending on the oxygen vacancy rate in a reducing atmosphere and temperature increase. This is related to the lattice structural defects of CeO_2 which implies the modifications formed by the electronic states between the valence and the conduction bands. The Urbach tail in the absorption spectrum indicates the presence of absorbing photons with energy lower than the optical gap (sub-bandgap absorption). It reflects the existence of disorders/defects, which induce the formation of mind gap states.

The correlation obtained between Vo^{-}, and grain size indicates that at the lowest value of the grain size of the particle, the highest oxygen vacancy and the highest defect concentration on the surface occur. Therefore, this curve will be useful to predict the behavior of several CeO_2 based samples.

In addition, the deposition of Au nanoparticles on the surface of CeO_2 allows to improve the properties formed by the electronic states between the valence band and the conduction band by increasing more than twice the structural defects compared to CeO_2 alone.

Acknowledgments

MXCG acknowledges a graduate fellowship from CONACYT (CVU-718943). This research has been supported by UAM-Iztapalapa (Project-2950101) with facilities provided by the laboratory of catalyst and advanced materials (T-256) and, special thanks to the XRD Laboratory (T-128) UAM-I, AAS Laboratory (T-255) UAM-I, and Raman Laboratory (G-010) UAM-A for the measurements, and to all the people who have made possible the culmination of this work amidst this complex times.

References

Abd El-Moemen, A., Abdel-Mageed, A. M., Bansmann, J., Parlinska-Wojtan, M., Behm, R. J., & Kučerová, G. (2016). Deactivation of Au/CeO_2 catalysts during CO oxidation:

Influence of pretreatment and reaction conditions. *Journal of Catalysis 341*, 160-179. https://doi.org/10.1016/j.jcat.2016.07.005

Acosta-Silva, Y. J., Toledano-Ayala, M., Torres-Delgado, G., Torres-Pacheco, I., Méndez-López, A., Castanedo-Pérez, R., & Zelaya-Ángel, O. (2019). Nanostructured CeO_2 thin films prepared by the sol-gel dip-coating method with anomalous behavior of crystallite size and bandgap. *Journal of Nanomaterials*, 2019. https://doi.org/10.1155/2019/5413134

Agarwal, S., Lefferts, L., Mojet, B. L., Ligthart, D. M., Hensen, E. J., Mitchell, D. R., ... & Datye, A. K. (2013). Exposed surfaces on shape-controlled ceria nanoparticles revealed through AC-TEM and water-gas shift reactivity. *ChemSusChem 6*(10), 1898-1906. https://doi.org/10.1002/cssc.201300651

Audebrand, N., Guillou, N., Auffrédic, J. P., & Louër, D. (1996). The thermal behaviour of ceric ammonium nitrate studied by temperature-dependent X-ray powder diffraction. *Thermochimica Acta 286*(1), 83-87. https://doi.org/10.1016/0040-6031(96)02944-9

Barton, D. G., Shtein, M., Wilson, R. D., Soled, S. L., & Iglesia, E. (1999). Structure and electronic properties of solid acids based on tungsten oxide nanostructures. *The Journal of Physical Chemistry B 103*(4), 630-640. https://doi.org/10.1021/jp983555d

Boubaker, K. (2011). A physical explanation to the controversial Urbach tailing universality. *The European Physical Journal Plus 126*(1), 1-4. https://doi.org/10.1140/epjp/i2011-11010-4

Centeno, M. A., Ramírez Reina, T., Ivanova, S., Laguna, O. H., & Odriozola, J. A. (2016). Au/CeO_2 catalysts: structure and CO oxidation activity. *Catalysts 6*(10), 158. https://doi.org/10.3390/catal6100158

Chang, M. W., & Sheu, W. S. (2016). Water-gas-shift reaction on reduced gold-substituted $Ce_{1-x}O_2$ (111) surfaces: the role of Au charge. *Physical Chemistry Chemical Physics 19*(3), 2201-2206. https://doi.org/10.1039/C6CP07185F

Choudhury, B., Chetri, P., & Choudhury, A. (2015). Annealing temperature and oxygen-vacancy-dependent variation of lattice strain, band gap and luminescence properties of CeO_2 nanoparticles. *Journal of Experimental Nanoscience 10*(2), 103-114. https://doi.org/10.1080/17458080.2013.801566

Coelho, A. A. (2018). TOPAS and TOPAS-Academic: an optimization program integrating computer algebra and crystallographic objects written in C++. *Journal of Applied Crystallography 51*(1), 210-218. https://doi.org/10.1107/S1600576718000183

da Silva, A. N., Pinto, R. C., Freire, P. T., Junior, J. A. L., Oliveira, A. C., & Josué Filho, M. (2015). Temperature and high-pressure effects on the structural features of catalytic nanocomposites oxides by Raman spectroscopy. *Spectrochimica Acta Part A: Molecular and Biomolecular Spectroscopy 138*, 763-773. https://doi.org/10.1016/j.saa.2014.11.081

Daniel, M., & Loridant, S. (2012). Probing reoxidation sites by *in situ* Raman spectroscopy: differences between reduced CeO_2 and Pt/CeO_2. *Journal of Raman Spectroscopy 43*(9), 1312-1319. https://doi.org/10.1002/jrs.4030

Deshpande, S., Patil, S., Kuchibhatla, S. V., & Seal, S. (2005). Size dependency variation in lattice parameter and valency states in nanocrystalline cerium oxide. *Applied Physics Letters 87*(13), 133113. https://doi.org/10.1063/1.2061873

Eustis, S., & El-Sayed, M. A. (2006). Why gold nanoparticles are more precious than pretty gold: noble metal surface plasmon resonance and its enhancement of the radiative and nonradiative properties of nanocrystals of different shapes. *Chemical Society Reviews 35*(3), 209-217. https://doi.org/10.1039/B514191E

Filtschew, A., Hofmann, K., & Hess, C. (2016). Ceria and its defect structure: new insights from a combined spectroscopic approach. *The Journal of Physical Chemistry C 120*(12), 6694-6703. https://doi.org/10.1021/acs.jpcc.6b00959

Freakley, S. J., He, Q., Kiely, C. J., & Hutchings, G. J. (2015). Gold catalysis: a reflection on where we are now. *Catalysis Letters 145*(1), 71-79. https://doi.org/10.1007/s10562-014-1432-0

Gunkel, F., Christensen, D. V., Chen, Y. Z., & Pryds, N. (2020). Oxygen vacancies: The (in) visible friend of oxide electronics. *Applied Physics Letters 116*(12), 120505. https://doi.org/10.1063/1.5143309

Guo, M., Lu, J., Wu, Y., Wang, Y., & Luo, M. (2011). UV and visible Raman studies of oxygen vacancies in rare-earth-doped ceria. *Langmuir 27*(7), 3872-3877. https://doi.org/10.1021/la200292f

Haruta, M. (1997). Size-and support-dependency in the catalysis of gold. *Catalysis Today 36*(1), 153-166. https://doi.org/10.1016/S0920-5861(96)00208-8

Haruta, M., Yamada, N., Kobayashi, T., & Iijima, S. (1989). Gold catalysts prepared by coprecipitation for low-temperature oxidation of hydrogen and of carbon monoxide. *Journal of Catalysis 115*(2), 301-309. https://doi.org/10.1016/0021-9517(89)90034-1

Hassanien, A. S., & Akl, A. A. (2016). Effect of Se addition on optical and electrical properties of chalcogenide CdSSe thin films. *Superlattices and Microstructures 89*, 153-169. https://doi.org/10.1016/j.spmi.2015.10.044

Hernández, J. A., Gómez, S. A., Zepeda, T. A., Fierro-González, J. C., & Fuentes, G. A. (2015). Insight into the deactivation of Au/CeO_2 catalysts studied by *in situ* spectroscopy during the CO-PROX reaction. *ACS Catalysis 5*(7), 4003-4012. https://doi.org/10.1021/acscatal.5b00739

Huang, X. S., Sun, H., Wang, L. C., Liu, Y. M., Fan, K. N., & Cao, Y. (2009). Morphology effects of nanoscale ceria on the activity of Au/CeO_2 catalysts for low-temperature CO oxidation. *Applied Catalysis B: Environmental 90*(1-2), 224-232. https://doi.org/10.1016/j.apcatb.2009.03.015

Karpenko, A., Leppelt, R., Plzak, V., & Behm, R. J. (2007). The role of cationic Au^{3+} and nonionic Au^0 species in the low-temperature water-gas shift reaction on Au/CeO_2 catalysts. *Journal of Catalysis 252*(2), 231-242. https://doi.org/10.1016/j.jcat.2007.09.017

Kosacki, I., Suzuki, T., Anderson, H. U., & Colomban, P. (2002). Raman scattering and lattice defects in nanocrystalline CeO_2 thin films. *Solid State Ionics 149*(1-2), 99-105. https://doi.org/10.1016/S0167-2738(02)00104-2

Lakshmanan, P., Averseng, F., Bion, N., Delannoy, L., Tatibouët, J. M., & Louis, C. (2013). Understanding of the oxygen activation on ceria-and ceria/alumina-supported gold catalysts: a study combining $^{18}O/^{16}O$ isotopic exchange and EPR spectroscopy. *Gold Bulletin 46*(4), 233-242. https://doi.org/10.1007/s13404-013-0103-z

Lee, Y., He, G., Akey, A. J., Si, R., Flytzani-Stephanopoulos, M., & Herman, I. P. (2011). Raman analysis of mode softening in nanoparticle $CeO_{2-\delta}$ and Au-$CeO_{2-\delta}$ during CO oxidation. *Journal of the American Chemical Society 133*(33), 12952-12955. https://doi.org/10.1021/ja204479j

Lykaki, M., Pachatouridou, E., Carabineiro, S. A., Iliopoulou, E., Andriopoulou, C., Kallithrakas-Kontos, N., & Konsolakis, M. (2018). Ceria nanoparticles shape effects on the structural defects and surface chemistry: Implications in CO oxidation by Cu/CeO_2 catalysts. *Applied Catalysis B: Environmental 230*, 18-28. https://doi.org/10.1016/j.apcatb.2018.02.035.

Ovando-Medina, V. M., Farías-Cepeda, L., Pérez-Aguilar, N. V., de la Rosa, J. R., Martínez-Gutiérrez, H., Romero-Galarza, A., & Cayetano-Castro, N. (2018). Facile synthesis of low band gap ZnO microstructures. *Revista Mexicana de Ingeniería Química 17*(2), 455-462. https://doi.org/10.24275/10.24275/uam/izt/dcbi/revmexingquim/2018v17N2/Ovando

Padilla-Rosales, I., López-Juárez, R., López-Pacheco, G., Falcony, C., & González, F. (2020). Near infrared photon-downshifting in Yb^{3+}– doped titanates: The influence of intrinsic defects. *Journal of Alloys and Compounds 834*, 155081. https://doi.org/10.1016/j.jallcom.2020.155081

Pushkarev, V. V., Kovalchuk, V. I., & d'Itri, J. L. (2004). Probing defect sites on the CeO_2 surface with dioxygen. *The Journal of Physical Chemistry B 108*(17), 5341-5348. https://doi.org/10.1021/jp0311254

Reina, T. R., Ivanova, S., Delgado, J. J., Ivanov, I., Idakiev, V., Tabakova, T., & Odriozola, J. A. (2014). Viability of Au/CeO_2-ZnO/Al_2O_3 catalysts for pure hydrogen production by the water-gas shift reaction. *Chem Cat Chem 6*(5), 1401-1409. https://doi.org/10.1002/cctc.201300992

Rösken, L. M., Körsten, S., Fischer, C. B., Schönleber, A., van Smaalen, S., Geimer, S., & Wehner, S. (2014). Time-dependent growth of crystalline Au^0-nanoparticles in cyanobacteria as self-reproducing bioreactors: 1. *Anabaena* sp. *Journal of Nanoparticle Research 16*(4), 1-14. https://doi.org/10.1007/s11051-014-2370-x

Sartoretti, E., Novara, C., Giorgis, F., Piumetti, M., Bensaid, S., Russo, N., & Fino, D. (2019). *in situ* Raman analyses of the soot oxidation reaction over nanostructured ceria-based catalysts. *Scientific Reports 9*(1), 1-14. https://doi.org/10.1038/s41598-019-39105-5

Sartoretti, E., Novara, C., Fontana, M., Giorgis, F., Piumetti, M., Bensaid, S., Russo, N., & Fino, D. (2020). New insights on the defect sites evolution during CO oxidation over doped ceria nanocatalysts probed by *in situ* Raman spectroscopy. *Applied Catalysis A 596*, 117517. https://doi.org/10.1016/j.apcata.2020.117517

Schilling, C., & Hess, C. (2018). Real-time observation of the defect dynamics in working Au/CeO_2 catalysts by combined operando Raman/UV-Vis spectroscopy. *The Journal of Physical Chemistry C 122*(5), 2909-2917. https://doi.org/10.1021/acs.jpcc.8b00027

Schoonheydt, R. A. (2010). UV-VIS-NIR spectroscopy and microscopy of heterogeneous catalysts. *Chemical Society Reviews 39*(12), 5051-5066. https://doi.org/10.1039/C0CS00080A

Thill, A. S., Lobato, F. O., Vaz, M. O., Fernandes, W. P., Carvalho, V. E., Soares, E. A., ... & Bernardi, F. (2020). Shifting the band gap from UV to visible region in cerium oxide nanoparticles. *Applied Surface Science 528*, 146860. https://doi.org/10.1016/j.apsusc.2020.146860

Tiwari, S., Khatun, N., Patra, N., Yadav, A. K., Bhattacharya, D., Jha, S. N., ... & Sen, S. (2019). Role of oxygen vacancies in Co/Ni Substituted CeO_2: A comparative study. *Ceramics International 45*(3), 3823-3832. https://doi.org/10.1016/j.ceramint.2018.11.053

Trogadas, P., Parrondo, J., & Ramani, V. (2012). CeO_2 surface oxygen vacancy concentration governs *in situ* free radical scavenging efficacy in polymer electrolytes. *ACS Applied Materials & Interfaces 4*(10), 5098-5102. https://doi.org/10.1021/am3016069

Trovarelli, A., & Fornasiero, P. (2013). *Chemical Physics and Chemistry: Catalysis by ceria and related materials*. (Vol. 12). World Scientific, Singapore. Pp.4-909

Varez, A., Garcia-Gonzalez, E., & Sanz, J. (2006). Cation miscibility in CeO_2-ZrO_2 oxides with fluorite structure. A combined TEM, SAED and XRD Rietveld analysis. *Journal of Materials Chemistry 16*(43), 4249-4256. https://doi.org/10.1039/B607778A

Vindigni, F., Manzoli, M., Damin, A., Tabakova, T., & Zecchina, A. (2011). Surface and inner defects in Au/CeO_2 WGS catalysts: Relation between Raman properties, reactivity, and morphology. *Chemistry-A European Journal 17*(16), 4356-4361. https://doi.org/10.1002/chem.201003214

Weber, W. H., Hass, K. C., & McBride, J. R. (1993). Raman study of CeO_2: Second-order scattering, lattice dynamics, and particle-size effects. *Physical Review B 48*(1), 178. https://doi.org/10.1103/PhysRevB.48.178

Widmann, D., Leppelt, R., & Behm, R. J. (2007). Activation of a Au/CeO_2 catalyst for the CO oxidation reaction by surface oxygen removal/oxygen vacancy formation. *Journal of Catalysis 251*(2), 437-442. https://doi.org/10.1016/j.jcat.2007.07.026

Willets, K. A., & Van Duyne, R. P. (2007). Localized surface plasmon resonance spectroscopy and sensing. *Annual Reviews of Physical Chemistry 58*, 267-297. https://doi.org/10.1146/annurev.physchem.58.032806.104607

Yaghoubi, H., Li, Z., Chen, Y., Ngo, H. T., Bhethanabotla, V. R., Joseph, B., ... & Takshi, A. (2015). Toward a visible light-driven photocatalyst: the effect of midgap-states-induced energy gap of undoped TiO_2 nanoparticles. *ACS Catalysis 5*(1), 327-335. https://doi.org/10.1021/cs501539q

Zhang, R. R., Ren, L. H., Lu, A. H., & Li, W. C. (2011). Influence of pretreatment atmospheres on the activity of Au/CeO_2 catalyst for low-temperature CO oxidation. *Catalysis Communications 13*(1), 18-21. https://doi.org/10.1016/j.catcom.2011.06.013

Ziemba, M., Ganduglia-Pirovano, M. V., & Hess, C. (2021). Insight into the mechanism of the water-gas shift reaction over Au/CeO_2 catalysts using combined operando spectroscopies. *Faraday Discussions 229*, 232-250. https://doi.org/10.1039/C9FD00133F